

# Contents

<b>I</b>	<b>ActiveAx</b>	<b>3</b>
<b>1</b>	<b>Diffusion MRI protocols for single fibre structures</b>	<b>5</b>
1.1	Protocol optimisation . . . . .	6
1.2	Experiments . . . . .	11
1.3	Results . . . . .	14
1.4	Discussion . . . . .	18
	Appendix 1.A Protocols . . . . .	22



**Part I**

**ActiveAx**



## Chapter 1

# Optimized diffusion MRI protocols for estimating axon diameter with known fibre orientation

In the previous chapters we have investigated two very different techniques in Diffusion Tensor Imaging (DTI) and  $q$ -space imaging (QSI). DTI only requires relatively little amounts of data, but it's underlying model is based on the assumption that all observed diffusion is Gaussian. Clearly, this is a gross oversimplification of the complex diffusion mechanisms present in biological tissue. QSI on the other hand makes no assumption about the diffusion process and can theoretically reveal even the most complex diffusion displacement profiles. QSI generally requires large amounts of data and requires very strong diffusion gradients. Henceforth, the implementation of true QSI on clinical systems is very difficult and the derived parameters are often difficult to interpret (see Chapter ??).

In the following chapters we will investigate a different model-based diffusion imaging technique, which can be seen as a compromise between the simple model of DTI and the complex QSI approach. Here, our work is heavily based on the ActiveAx approach by Alexander (2008), who used a simple compartment tissue model to derive axon diameter and axon density indices in the brain using standard clinical hardware (see Chapter ??).

Alexander's work is designed under the premise of full brain imaging and therefore he presents DWI protocols that work independently of the fibre orientation. We call this the orientation invariant ( $\mathcal{OI}$ ) approach. The  $\mathcal{OI}$  approach is based on acquiring multiple HARDI shells and requires good angular resolution to retain the orientation invariant features. As a consequence, the  $\mathcal{OI}$  protocols used e.g. in (Alexander et al., 2010) require scan times of more than 1h, which limits their transition to clinical practise.

The main motivation of this work is to reduce the scan time of the ActiveAx protocols to a more clinically applicable limit of 20-30 minutes. The central idea

to attain this reduction is to discard the requirement for orientational invariance and focus on structures with a coherent known single fibre orientation. Many studies before have focussed on those single fibre structures (e.g. corpus callosum (CC) or spinal cord (SC)) as they can be expressed in terms of relatively simple models, without the need to include complex fibre configurations such as multiple fibre crossings, bending or fanning. Furthermore, many single fibre structures such as CC and SC are of great importance to many developmental and pathological processes. Our approach makes imaging these structures more practicable with a 20-30 minute time frame, where a >1h full-brain protocol might not be feasible.

In this chapter, we present a modification to the existing protocol optimization framework of Alexander (2008) (see Section ??) that incorporates this *a-priori* information about fibre organisation. We refer to this approach and its resulting protocols as the single-fibre ( $\mathcal{SF}$ ) method. We evaluate different  $\mathcal{SF}$  implementations and use computer simulations to test and compare the  $\mathcal{SF}$  method to the  $\mathcal{OI}$  approach. By design, the  $\mathcal{SF}$  is optimised only for a specific predetermined fibre orientation. However, in reality there will always be some variation even in very coherently aligned white matter (WM) tracts. We therefore test how much influence this variation has on our  $\mathcal{SF}$  approach compared to  $\mathcal{OI}$ . Finally, we implemented the  $\mathcal{SF}$  protocol to demonstrate its feasibility within a real biological tissue sample of fixed cervical monkey SC. Although this study is motivated by improving in-vivo clinical applicability, we chose to first test our approach on a pre-clinical scanner on a fixed tissue sample to avoid the challenges of in-vivo scanning (e.g. motion and insufficient image resolution) and focus on an initial demonstration of our method. The results and observations made in this chapter form the basis of the subsequent in-vivo implementation we present in the following chapter.

## 1.1 Protocol optimisation

This section discusses how we adapt the  $\mathcal{OI}$  optimisation of Alexander (2008) to the  $\mathcal{SF}$  case. The original  $\mathcal{OI}$  optimisation is designed to determine the best PGSE pulse parameters (i.e. diffusion gradient strength ( $|G|$ ), diffusion gradient pulse duration ( $\delta$ ), diffusion time ( $\Delta$ )) for a fixed number  $M$  of shells, each including a fixed number  $N$  of distributed gradient directions. The gradient directions scheme in the  $\mathcal{OI}$  approach is fixed and uniformly distributed over the sphere as in (Cook et al., 2007). The HARDI-like gradient scheme is necessary to guarantee orientational invariance, i.e. be sensitive to restriction regardless of diffusion direction. In our  $\mathcal{SF}$  implementation we can assume a known diffusion direction and therefore do not require the uniform angular sampling of the  $\mathcal{OI}$  approach. This allows us to include the gradient scheme together with the PGSE pulse setting in the optimisation process. In addition to  $\mathcal{SF}$ , which optimises gradient scheme and PGSE pulse parameters simultaneously, we are also interested in how much the optimisation of the gradient scheme ( $\mathcal{SF}_{dirs}$ ) alone and the PGSE parameters alone ( $\mathcal{SF}_{pulses}$ ) has on the performance of the resulting protocols. In total we tested the four following different variants of Alexander (2008)’s optimisation framework:

- $\mathcal{OI}$ :** The orientationally invariant protocol optimisation as described in (Alexander, 2008).
- $\mathcal{SF}$ :** The adapted algorithm optimises both the PGSE parameters and gradient direction scheme for  $M$  shells assuming a single *a-priori* known fibre direction.
- $\mathcal{SF}_{pulses}$ :** Similar to the  $\mathcal{OI}$  optimisation approach, the algorithm uses a fixed gradient scheme for each of the  $M$  shells and only optimises the PGSE pulse parameters. The main difference to  $\mathcal{OI}$  is that the algorithm optimises for a single *a-priori* known fibre direction instead of a set of ‘worst case’ fibre directions.
- $\mathcal{SF}_{dirs}$ :** This is a two-step optimisation approach. The  $\mathcal{SF}_{pulses}$  algorithm is performed to determine the best  $M$  PGSE pulse settings. In a second step the gradient scheme for each of the each  $M$  shells are optimised, keeping the PGSE pulse parameters fixed.

Table 1.1 summarises the optimisation parameters for each of the four algorithms. It is important to note that the inclusion of the optimisation of individual gradient directions in  $\mathcal{SF}_{dirs}$  and  $\mathcal{SF}$  drastically increases the number of free parameters to be optimised from  $O(M)$  to  $O(N \cdot M)$  compared to  $\mathcal{OI}$  and  $\mathcal{SF}_{pulses}$ .

Table 1.1: Overview of parameters for the tested protocol optimisation approaches.

Protocol name	$\mathcal{OI}$ (orientation invariant)	$\mathcal{SF}$ (pulses + directions)	$\mathcal{SF}_{pulses}$ (pulses only)	$\mathcal{SF}_{dirs}$ (directions only)
Free parameters	$\delta_m, \Delta_m, G_m$	$\phi_{m,n}, \theta_{m,n}$ $\delta_m, \Delta_m, G_m$	$\delta_m, \Delta_m, G_m$	$\phi_{m,n}, \theta_{m,n}$
Fixed parameters	$\phi_n, \theta_n$	–	$\phi_n, \theta_n$	$\delta_m, \Delta_m, G_m$
Specific fibre direction	no	yes	yes	yes
No. of free parameters	$O(M)$	$O(M \times N)$	$O(M)$	$O(M \times N)$

### 1.1.1 Tissue model

Like (Alexander, 2008), we use a simple two-compartment model of white matter tissue, with axons represented as cylinders with a single radius and extra-axonal tissue represented by an axially symmetric diffusion tensor (‘ZeppelinCylinder’ in the taxonomy of Panagiotaki et al. (2012)). For the optimisation we assume tissue diffusion properties typically found in *in-vivo* human white matter. A full list of the model parameters used in the optimisation is given in Table 1.2.

### 1.1.2 Implementation

We implement the four algorithms as described in Section ?? for  $M = 8$  different sets of PGSE parameters. For  $\mathcal{OI}$  and  $\mathcal{SF}_{pulses}$  we use the default setting for the SOMA algorithm, i.e., 500 migration steps with 100 migrating individuals.

Table 1.2: Model parameters used for optimisation.

Cylinder (intra-axonal)		Axially symmetric tensor (extra-axonal)	
$f_{intra}$	0.7	$f_{extra}$	0.3
$D_{\parallel}$	$1.7 \cdot 10^{-9} \text{ s/mm}^2$	$D_{\parallel}$	$1.7 \cdot 10^{-9} \text{ m}^2/\text{s}$
$D_{\perp}$	$6 \cdot 10^{-10} \text{ s/mm}^2$	$D_{\perp}$	$6 \cdot 10^{-10} \text{ s/m}^2/\text{s}$
dir	$[0, 0, 1]^T$	dir	$[0, 0, 1]^T$
R	$\{1..10\} \mu\text{m}$		

For  $\mathcal{SF}_{dirs}$  and  $\mathcal{SF}_{pulses}$ , the parameter space to explore is much larger and we are using 1000 individuals with 750 migration steps to ensure convergence. To avoid local minima, each optimisation is repeated 5 times and from the resulting protocols the one with the smallest CRLB is chosen. The available gradient strength is limited to 60mT/m to simulate a typical clinical MRI scanner.

### 1.1.3 Optimised protocols

Figure 1.2 shows the CRLB of the four different optimisation for different  $N$ . We can see that CRLB distinguishes the four protocols in two groups:  $\mathcal{OI}/\mathcal{SF}_{pulses}$  with fixed directions and  $\mathcal{SF}_{dirs}/\mathcal{SF}$  with optimised directions.  $\mathcal{SF}_{dirs}$  and  $\mathcal{SF}$  consistently produce lower CRLB than  $\mathcal{OI}$  and  $\mathcal{SF}_{pulses}$  regardless of the chosen  $N$ , although the differences between the two groups become smaller for larger  $N > 60$ . For better comparison, Figure 1.2 shows the corresponding  $N$  for a different values of CRLB. We can see that  $\mathcal{SF}$  and  $\mathcal{SF}_{dirs}$  both achieve the same CRLB values of  $\mathcal{OI}$  with significantly less directions. In other words, the  $\mathcal{SF}_{dirs}$  and  $\mathcal{SF}$  promise a comparable performance to  $\mathcal{OI}$  with only 25%–33% the amount of data required.

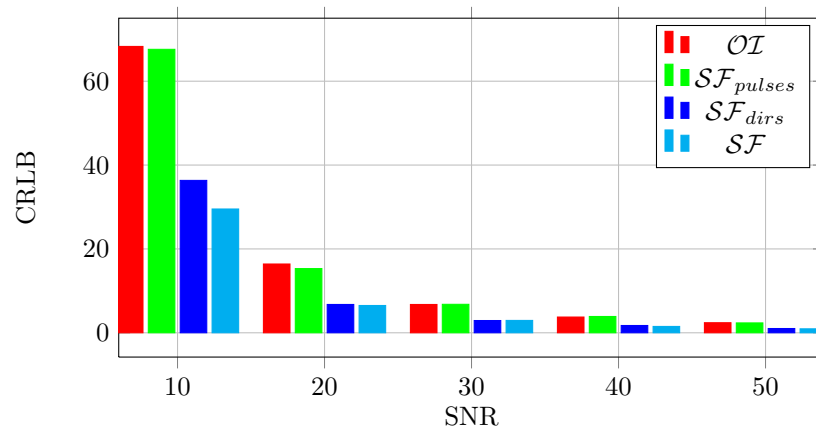


Figure 1.1: CRLBs of optimised protocols under different SNR.

Figure 1.1 shows the CRLB of the four different optimisations for a fixed



$N = 90$  but different SNR conditions. The results here are very similar to the findings shown above. Both  $\mathcal{SF}$  and  $\mathcal{SF}_{dirs}$  consistently show CRLB values three to four times lower than those of  $\mathcal{OI}$  and  $\mathcal{SF}_{pulses}$  for similar SNR values. The differences are most apparent for low SNR values, which are also more common in real clinical diffusion MRI.

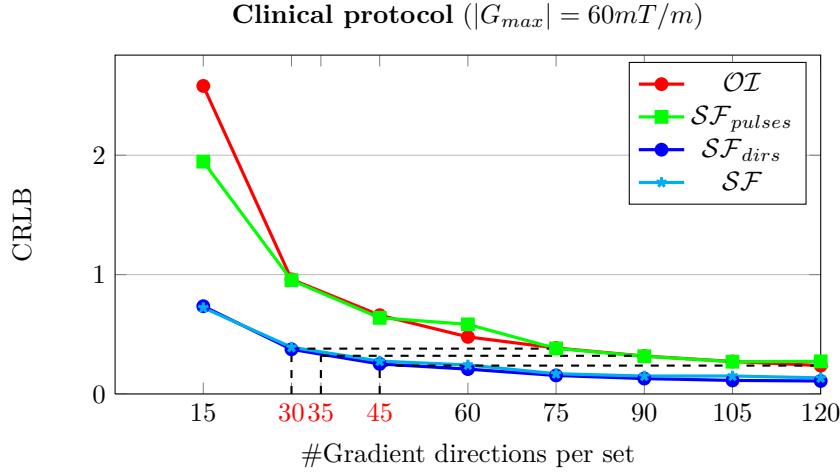


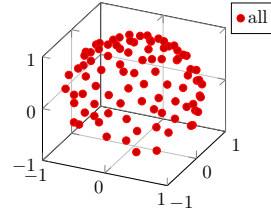
Figure 1.2: CRLBs of optimised protocols with different  $N$  number of gradient directions.

Table 1.3 shows an example of the  $\mathcal{OI}$  and  $\mathcal{SF}$  protocols variants we obtain for  $N = 90$  and SNR= 20. A more comprehensive visualisation of the different protocol parameters can be found in Appendix 1.A.1. We deliberately chose a large number of  $M$  to reevaluate the optimal number of different PGSE for each protocol. Our findings here confirm the results of (Alexander, 2008), which suggest that a smaller number of  $M = 4$  suffices to capture all unique combinations of PGSE pulse parameters. We also note that  $\mathcal{OI}$  and  $\mathcal{SF}_{pulses}$  protocols are almost identical, which suggest that the choice of diffusion orientation for the  $\mathcal{OI}$  has little influence on the outcome of the algorithm.

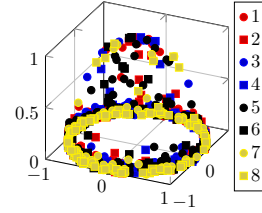
Table 1.3: Protocol parameters and gradient schemes for  $N = 90$ ,  $M = 8$ . The  $M$  different gradient direction schemes are coded by different colors. Please note that in the  $\mathcal{OI}$  and  $\mathcal{SF}_{pulses}$  protocols all  $M$  gradient direction schemes are identical.

(a)  $\mathcal{OI}$  protocol

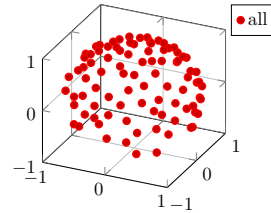
$\delta$ [ms]	$\Delta$ [ms]	$ G $ [mT/m]	$b$ -value [s/mm <sup>2</sup> ]
12.9	17.9	60	583
12.9	17.9	60	585
12.9	17.9	60	587
12.9	17.9	60	588
22.7	48.3	30	1480
24.4	46.6	30	1684
26.3	44.7	40	2752
33	38	60	7585

(b)  $\mathcal{SF}$  protocol

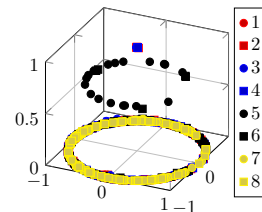
$\delta$ [ms]	$\Delta$ [ms]	$ G $ [mT/m]	$b$ -value [s/mm <sup>2</sup> ]
14.7	19.8	60	832
14.8	19.8	60	837
15.1	20.1	60	883
15.4	20.4	60	932
21.2	53.9	30	1361
27.2	47.9	40	3123
27.9	47.2	40	3452
35	40	60	8974

(c)  $\mathcal{SF}_{pulses}$  protocol

$\delta$ [ms]	$\Delta$ [ms]	$ G $ [mT/m]	$b$ -value [s/mm <sup>2</sup> ]
12.8	17.8	60	572
12.9	17.9	60	580
12.9	17.9	60	580
12.9	17.9	60	582
21.9	48.9	30	1484
24.7	46	30	1677
26.3	44.5	40	2639
32.9	37.9	60	7515

(d)  $\mathcal{SF}_{dirs}$  protocol

$\delta$ [ms]	$\Delta$ [ms]	$ G $ [mT/m]	$b$ -value [s/mm <sup>2</sup> ]
12.8	17.8	60	572
12.9	17.9	60	580
12.9	17.9	60	580
12.9	17.9	60	582
21.9	48.9	30	1484
24.7	46	30	1677
26.3	44.5	40	2639
32.9	37.9	60	7515



## 1.2 Experiments

### 1.2.1 Synthetic data

From all protocols for  $N = 90$  and  $SNR = 20$  we generate synthetic datasets, with which we then test and compare the performance of the different protocol optimisations. The number of gradient directions was chosen rather large to allow sufficient angular resolution for  $\mathcal{OI}$  and  $\mathcal{SF}_{dirs}$  protocols.

. The MR signals are generated from the same tissue model and tissue diffusion properties we used for the protocol optimisation (see section ?? and Table ?? for details). We use the Camino software package (Cook et al., 2006) to simulate datasets for four different cylinder radii  $R = 1, 2, 5, 10\mu m$  as a representation of radii usually found in *in-vivo* white matter tissue. To simulate noise in the MR acquisition, we add Rician noise with  $SNR = 20$  to the simulated noise-free datasets. To concentrate on comparing the estimates of radius and volume fraction between the protocols we assume all cylinders to be perfectly aligned along the  $[0, 0, 1]^T$  as assumed in the optimisation process.

#### Effect of principle diffusion direction

Even in very coherent structures such as the CC, the observed fibre direction is subject to some variation. However the protocols  $\mathcal{SF}$  and  $\mathcal{SF}_{dirs}$  contain gradient schemes designed for a fixed principle diffusion direction. To test the effect of potential misalignment between assumed and true principal diffusion direction we design the following experiment:

We create similar dataset as above, with the exception of varying the principal diffusion direction for each synthetic sample. Using the spherical representation of the cylinder direction, we sample each combination of polar angle  $\phi \in \{0..90\}^\circ$  and azimuth angle  $\theta \in \{0..180\}^\circ$  in discrete steps of  $5^\circ$ . In total we simulate 703 unique datasets with different principal diffusion directions (see Figure 1.3 for a plot of the generated diffusion directions).

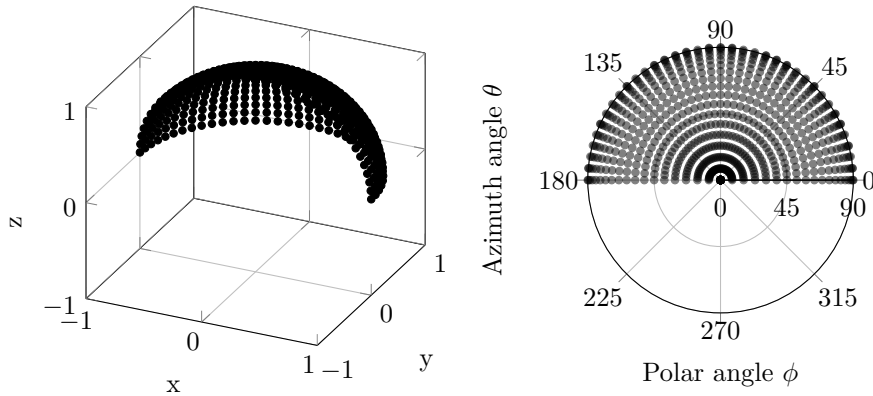


Figure 1.3: Generated diffusion directions to test orientation bias as 3-d scatter plot (left panel) and polar scatter plot (right panel).

### Dispersion

The dispersion of fibres is another confounding factor that has considerable influence on the estimates of cylinder radius and volume fraction Zhang et al. (2011). While (Zhang et al., 2011) also showed that the effect in coherent structures with moderate dispersion, such as in the CC, is negligible for  $\mathcal{OI}$ , it is unclear whether this is still the case for the optimised gradient schemes used in our  $\mathcal{SF}$  and  $\mathcal{SF}_{dirs}$  protocols. We therefore created set of data to test the effect of dispersion on our protocols. To simulate different degrees of dispersed diffusion directions, we used the the Van-Mises-Fisher distribution  $p_d$ :

$$p_d(\mathbf{x}; \mu, \kappa) = \frac{\kappa}{2\pi(e^\kappa - e^{-\kappa})} (\kappa \mu^T \mathbf{x}), \quad (1.1)$$

which is defined for each point  $\mathbf{x} \in \mathbb{R}^2$  on the unit sphere with  $\mu$  being the mean distribution of the distribution, and  $\kappa$  being the scalar concentration parameter that controls the dispersion of the distribution. From  $p_d$  we sample 1000 directions, take the average of the noise-free MR signal generated from our tissue model, and then add Rician noise as described above. To simulate different degrees of dispersion we vary  $\kappa \in [2, 4, 8, \dots, 512]$  with fixed  $\mu = [0, 0, 1]^T$ . Figure 1.4 illustrates the sampled directions for each of the used  $\kappa$  values. For  $\kappa \rightarrow \infty$  the amount of dispersion becomes negligible and the simulation is equivalent to the fibre configuration in ??.

#### 1.2.2 Feasibility study on fixed monkey spinal cord

Scans were performed on an experimental 4.7 Tesla scanner (Varian Inc., Palo Alto, CA, USA) in collaboration with the Danish Research Centre for Magnetic Resonance (DRCMR). To make best use of the hardware, we carry out the protocol optimisation as described above but increase  $|G|_{max}$  to  $300 \text{ mT/m}$ . We also adjust for differences in tissue properties between live and fixed tissue, e.g. decreased diffusivity and shrinkage of axon diameters, based on preliminary DTI analysis of the tissue sample (see modified tissue parameters in Table 1.4). Scan time in this experiment was limited to 12h only. To retain acceptable image resolution and SNR within the given time frame, we reduced the number of acquisitions to  $M = 4$  and  $N = 30$ . Furthermore, we only had time to test the  $\mathcal{SF}$  protocol in this experiment. The resulting protocol is summarised in Table ?? and described more comprehensively in Appendix 1.A.2.

We used a volume coil for transmission and a homemade 20 mm surface coil was used as receive coil. The data was was acquired using a spin-echo sequence with single line readout and a conventional pulsed gradient spin-echo preparation (Stejskal & Tanner, 1965). TE/TR were 59/2000 ms, field of view (FoV) was  $10 \times 10 \text{ mm}^2$ . The matrix size was  $64 \times 64$  and was 2-D interpolated to  $128 \times 128$  leading to an axial in-plane resolution of  $79 \times 79 \mu\text{m}^2$ . To support the high in-plane resolution we acquire thick slices of 1.5mm to achieve acceptable signal-to-noise ratio (SNR) in our data. The protocol was repeated 4 times with a total imaging time of 13 h. The magnitude images of the four repeated measurements were averaged offline prior to analysis.

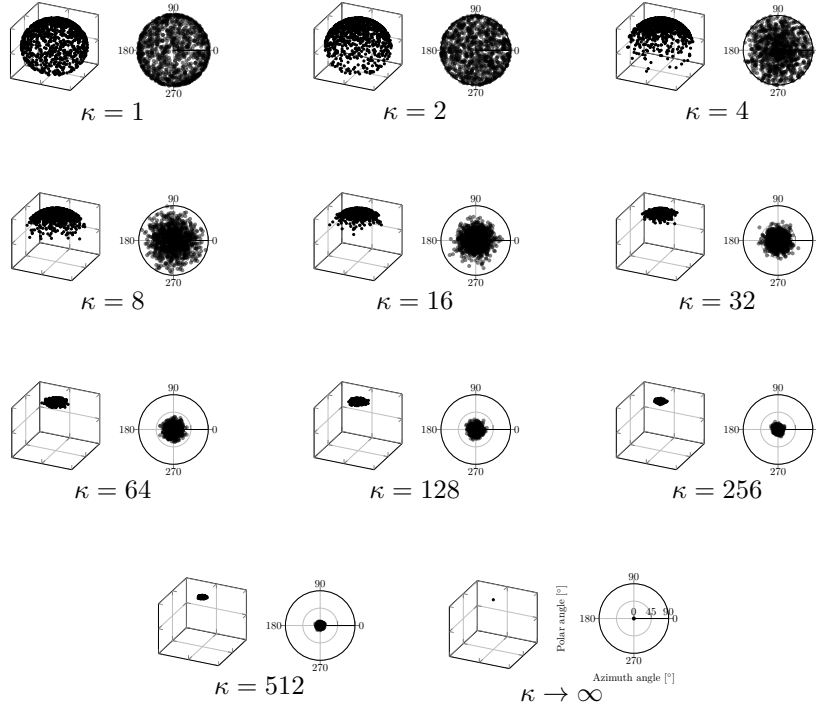


Figure 1.4: Visualisation of 1000 sample directions drawn from Von-Mises-Fisher distribution with varying  $\kappa$ . Left half of each figure shows the 3-d scatter plot, right half shows a polar plot of the sampled directions for each value of  $\kappa$ .

Table 1.4: Adjusted ex-vivo tissue model parameters used for pre-clinical scan optimisation (changes to in-vivo protocol are displayed in red).

Cylinder (intra-axonal)		Axially symmetric tensor (extra-axonal)	
$f_{intra}$	0.7	$f_{extra}$	0.3
$D_{\parallel}$	$4 \cdot 10^{-10} \text{ s/mm}^2$	$D_{\parallel}$	$4 \cdot 10^{-10} \text{ m}^2/\text{s}$
$D_{\perp}$	$2.5 \cdot 10^{-10} \text{ s/mm}^2$	$D_{\perp}$	$2.5 \cdot 10^{-10} \text{ s/m}^2/\text{s}$
dir	$[0, 0, 1]^T$	dir	$[0, 0, 1]^T$
R	$\{0.5, 1, 2\} \mu\text{m}$		

### 1.2.3 Model fitting

A voxel-wise fit of the MR signal is performed using a fitting method similar to (Alexander et al., 2010). We define the objective function as the maximum likelihood of model parameters given the observed MR signals under Rician noise ( $\sigma = 0.05$ ). We use the multi-run fitting routine of (Panagiotaki et al., 2012) to find an initial parameters, which determines the best parameter estimates

from multiple gradient-descend runs with perturbed starting points ( $n=20$  in our case). Based on the initial parameter estimates, we then perform a Markov chain Monte Carlo (MCMC) algorithm to determine the posterior distributions of the model parameters. To ensure convergence, we used the following, rather conservative setting for the MCMC algorithm: burn-in of 5000, sample interval of 1000, 5% parameter perturbations with uniform, uninformative priors.

To increase stability of the fitting we fix  $D_{\parallel}$  to its true value of  $1.7 \text{ mm/s}^2$  similar to previous studies (Assaf et al., 2008; Barazany et al., 2009; Alexander et al., 2010). Moreover,  $D_{\perp}$  is approximated by the tortuosity formulation of (Szafer et al., 1995):

$$D_{\perp} = f_{intra} \cdot D_{\parallel}.$$

For  $\mathcal{SF}_{dirs}$  and  $\mathcal{SF}$ , we also found our method to be very unstable with respect to determining the correct principal diffusion direction of the model, even when the fibre direction was close to  $[0, 0, 1]^T$ . This likely stems from the fact that the initial guess of the direction is computed from the Diffusion Tensor (DT) model. While this method works fine for  $\mathcal{OT}$  and  $\mathcal{SF}_{pulses}$  protocols, it fails when using the optimised gradient direction sets of  $\mathcal{SF}_{dirs}$  and  $\mathcal{SF}$ . We therefore fix the principal fibre direction to  $[0, 0, 1]^T$  in all experiments, unless stated otherwise.

### Fixed tissue

We chose to scan a sample of fixed monkey cervical spinal cord to test our protocol in a real biological system. The details of the sample preparation are described in (?). For the fixed tissue we use a slightly modified fitting routine to account for the differences between fixed and live tissue. Here we fix  $D_{par}$  to  $0.45 \mu\text{m/mm}^2$ . The volume fraction of the restricted compartment  $f$  was constrained to be in the range of  $[0.5, 1.0]$ . We then In each voxel, the mean of the posterior distribution of  $R$  and  $f_{intra}$  are calculated. For consistency with indices derived from histological examination and also previous imaging studies e.g. (Alexander et al., 2010), maps of the axon diameter index  $D = 2 \cdot R$  and the axonal density index  $\rho = f_{intra}/\pi/R^2$  are reported.

## 1.3 Results

### 1.3.1 Accuracy and precision of parameter estimates

Figure 1.5 shows box plots of the fitted volume fraction  $f_{intra}$  and  $R$  for different cylinder radii.

definition

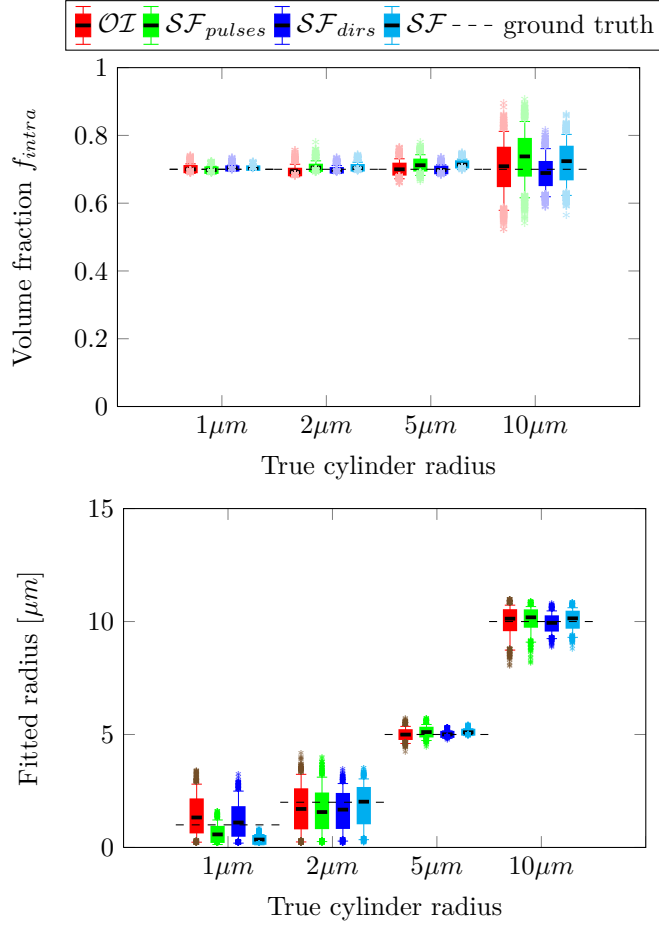
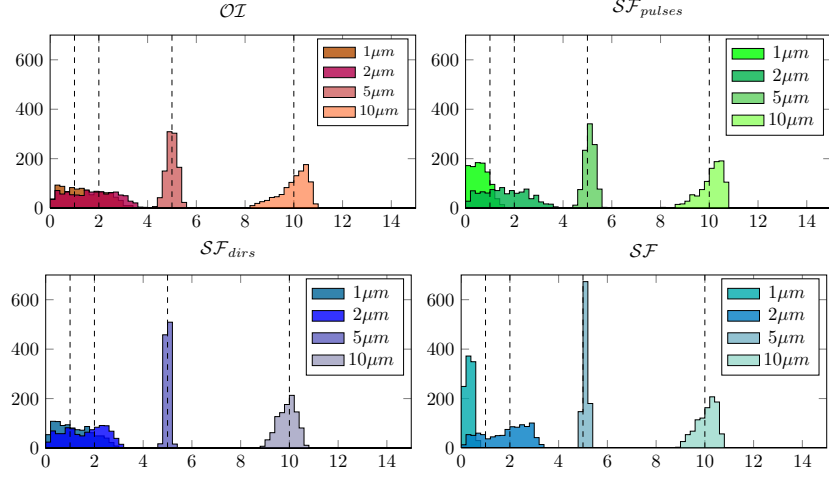


Figure 1.5: Boxplots of estimated  $f_{intra}$  and  $R$  for different cylinder radii.

All protocols can successfully recover the correct value for  $f_{intra}$  for all radii 1, 2 and 5  $\mu m$  with the posterior distributions being centred around the true value  $f_{intra} = 0.7$  with little variance.  $R = 10\mu m$  significantly more variance in the estimates is observed for in all protocols. Further we find also find the estimates to be less accurate, mainly in  $SF$  and  $SF_{pulses}$ , which overestimate of  $f_{intra}$  slightly.

Figure 1.6: Histograms of fitted cylinder radius  $R$  for different protocols.

Compared to  $f_{intra}$  results, we observe more variance in the posterior distributions of  $R$  estimates for all protocols. Over all  $R$   $SF_{dirs}$  and  $SF$  appear to achieve better results than  $OI$  and  $SF_{pulses}$  protocols. To illustrate this better, Figure 1.6 shows the posterior distributions of  $R$  for each protocol in more detail.

All protocols perform the best for  $R = 5\mu m$  with tight posterior distributions centred around the ground truth. While generally all protocols show very good accuracy in estimating  $R$ ,  $SF_{dirs}$  and  $SF$  have the advantage in terms of precision as their distributions are considerably tighter than for  $OI$  and  $SF_{pulses}$ . Compared to  $R = 5\mu m$ ,  $R = 10\mu m$  estimates generally are broader and with a notable negative skew, particularly for  $OI$  and  $SF_{pulses}$  protocols. As for  $5\mu m$ ,  $SF_{dirs}$  and  $SF$  produce more sharp parameter distributions than  $OI$  and  $SF_{pulses}$ , although the difference is less obvious. The broader distributions for  $R = 10\mu m$  might be explained by the long diffusion, which are necessary to estimate large radii accurately. We assume a typical T2 signal decay of 70ms in this experiment. As shown in (?), in this regime long diffusion times can not be reached with acceptable SNR. As a consequence, for  $R = 10m$  a greater proportion of the signal will appear unrestricted and causes the underestimation of  $f_{intra}$  and larger variation in radius estimates in our results.

Smaller radii  $R = 1\mu m$  and  $R = 2\mu m$  less well distinguished from each other in all protocols, with posterior distributions showing significant overlap as expected from limited gradient strength used in this experiment (Alexander, 2008; Alexander et al., 2010; Siow et al., 2012). For small radii the centre-of-mass (COM) effect on small radii prohibits any contrast between different  $R$ , which we find reflected in our posterior distributions (see Chapter ?? for a detailed explanation). However,  $SF$  suffers least from this and clearly outperforms the other protocols as it allows much better distinction between the small radii.

### 1.3.2 Variation of fibre direction

Figure 1.7 shows the root mean squared error for both  $f_{intra}$  and  $R$  parameters with respect to the principle orientation of diffusion for cylinders with small



radius  $R = 2\mu m$  and large radius  $R = 5\mu m$ . As in the previous experiment, all the protocols generally perform better for  $R = 5\mu m$  than  $R = 2\mu m$ . Therefore, the most marked differences between protocols appear in the  $R = 2\mu m$  dataset.

The plots clearly show that estimates of  $f_{intra}$  are unaffected by the true diffusion orientation in all protocols for  $R = 2\mu m$ . While this is expected for  $\mathcal{OI}$  and  $\mathcal{SF}_{pulses}$ , we can explain the performance of  $\mathcal{SF}$  and  $\mathcal{SF}_{dirs}$  explained by the small cylinder radius, which allows  $\mathcal{SF}$  and  $\mathcal{OI}$  to distinguish hindered and restricted diffusion even when the gradient scheme is not aligned perpendicular to the intra-axonal compartment. Results for  $R = 5\mu m$  show that  $f_{intra}$  estimates are affected more by the misalignment of the gradient scheme with larger radii, although the estimation error still remains low over all different directions.

Bigger differences between the protocols can be seen in the  $R$  estimation error. Again,  $\mathcal{OI}$  and  $\mathcal{SF}_{pulses}$  are consistent over the whole range of simulated fibre directions, with no apparent directional pattern of the estimation error. In contrast,  $\mathcal{SF}$  and  $\mathcal{SF}_{dirs}$  performance is considerably more impeded for larger misalignment of gradient scheme and cylinder orientation. The maximum estimation error is observed for rotation angles around  $45^\circ$ . With  $\phi$  close to  $90^\circ$ , the  $\mathcal{SF}$  and  $\mathcal{SF}_{dirs}$  gradient direction scheme now features more measurements perpendicular and parallel to the cylinder compartment, which reduces again the fitting error. For smaller misalignments of  $\phi < 15^\circ$  both  $\mathcal{SF}/\mathcal{SF}_{dirs}$  perform very similar to the  $\mathcal{OI}/\mathcal{SF}_{pulses}$  protocols.

**Effect of fibre dispersion:** Figure 1.8 shows the fitted  $f_{intra}$  and  $R$  estimates different degrees of intra-voxel dispersion of fibre orientations. For small  $\kappa$ , i.e. high degrees of dispersion, we observe large errors in estimates of both  $f_{intra}$  and  $R$ , as expected e.g. from (Zhang et al., 2011). However, for  $\kappa \geq 64$ , the fitted parameters converge to their respective ground truth, despite a considerable degree of dispersion still present in those datasets. With increasing  $\kappa$ , there appears to be no noticeable difference between the four protocols.

### 1.3.3 Proof-of-concept implementation

Figure 1.9 presents maps of axon diameter  $D$  and axonal density  $\rho$  in the upper cervical spinal cord obtained from the  $\mathcal{SF}$  protocol. We can discriminate well differences in axon diameter and axonal density indices between anatomically different white matter tracts. Dorsal and lateral sensory tracts show small axons diameters between  $1\text{--}4\mu m$  and a density of  $0.03\text{--}0.08\mu m^{-2}$ . The smallest axon calibers ( $<1.5\mu m$ ) are observed in the dorsal columns (DC) while mean axon size in the anterolateral column (ALC) is  $1.5\text{--}2.5\mu m$ . The largest axons ( $3\text{--}4\mu m$ ) are found in the corticospinal tracts (CST) together with low density of  $0.01\text{--}0.02\mu m^{-2}$ . Overall, we clearly observe left-right symmetry of axon diameter and density in all tracts, which corresponds well with the known anatomical organisation of the the SC. Parameters are also consistent along the SC within the limits of anatomical variation and are in the range of values reported in previous histological evaluation of the cord (Golabchi et al., 2010).

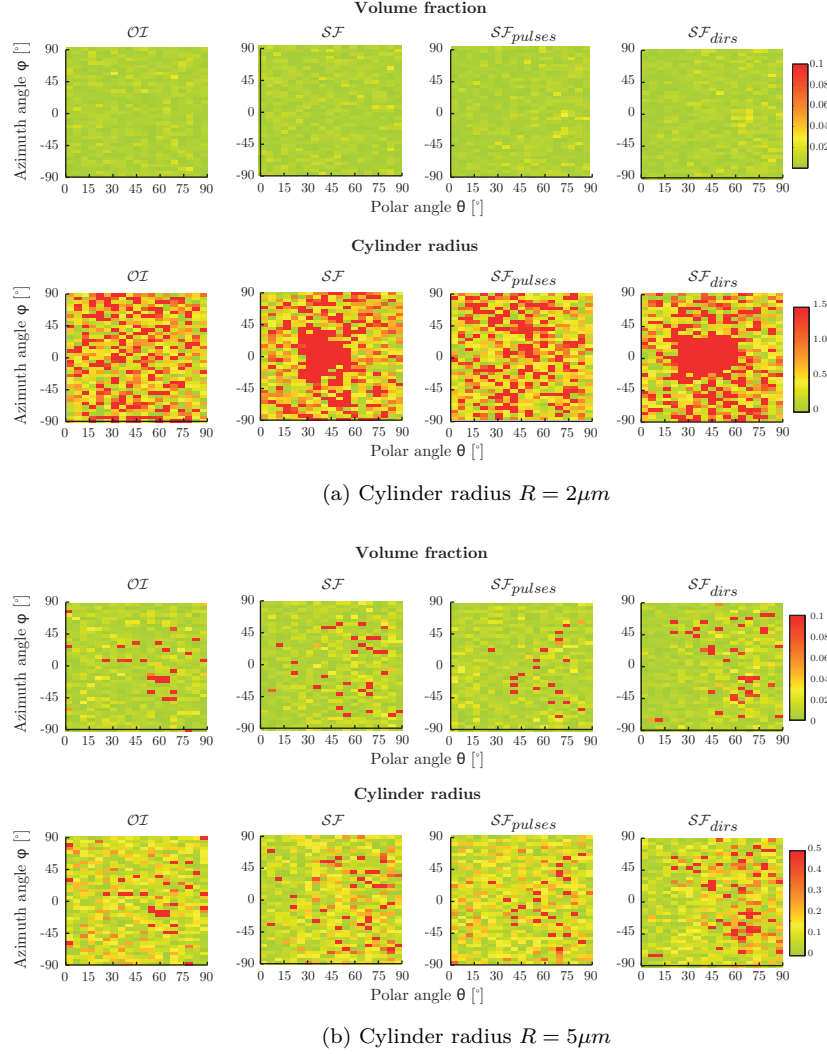


Figure 1.7: Root mean square error of  $f_{intra}$  and  $R$  estimates for different principle diffusion directions.

## 1.4 Discussion

We presented here a novel method that provides optimal diffusion weightings and gradient directions for estimating of axonal diameter by exploiting the single fibre orientation of structures like the corpus callosum or spinal cord. We demonstrated that the  $SF$  approach reduces the required amount of data by 60–75%, while achieving similar performance to  $OI$ . This translates into a considerable reduction in scan time from  $>1h$  for  $OI$  to less than 20–25 minutes, which makes routine clinical implementation much more viable.

Our results suggest that a dedicated optimisation of gradient directions is clearly beneficial over the orientation invariant  $OI$  approach, both in terms of

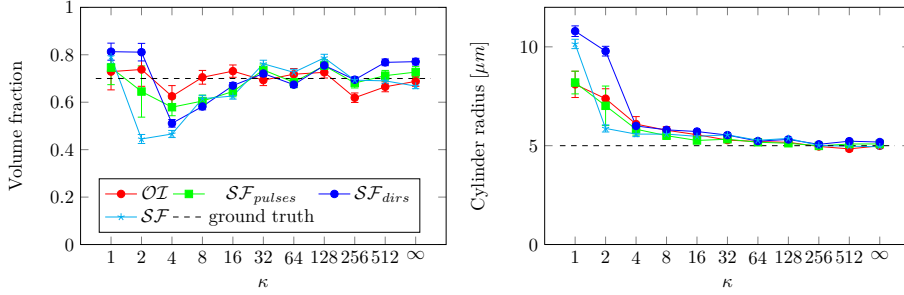


Figure 1.8: Mean and standard deviation of posterior distribution for fitted volume fraction and radius for different  $\kappa$  values.

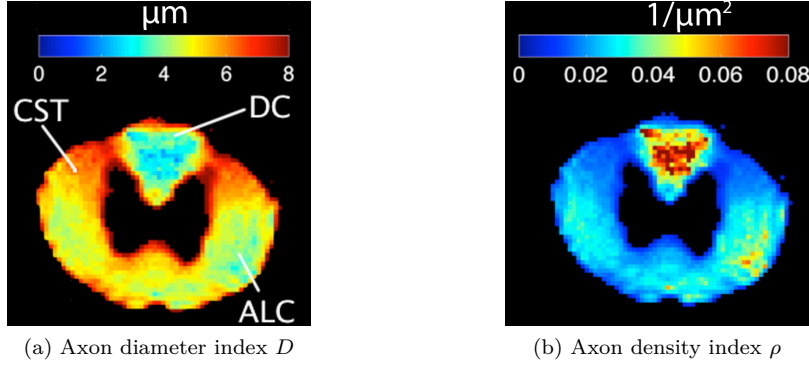


Figure 1.9: Axial slice of upper cervical cord showing maps of  $D$  and  $\rho$ . White markers show the approximate location of the corticospinal tracts (CST), anterolateral column (ALC) and dorsal column (DC)

CRLB and simulated noisy data when the fibre direction is known a-priori. We find that the optimisation routine deliberately diminishes angular resolution in favour of measuring diffusion only in the most informative directions (predominantly parallel and perpendicular to the WM tracts). We noticed that our optimised gradient scheme pick out predominantly gradient directions parallel and perpendicular to the cylinder compartment, presumably to maximise sensitivity to restricted diffusion. In that respect our automatically optimised gradient schemes agree with other many other studies e.g. (Stanisz et al., 1997; Avram et al., 2008; Assaf et al., 2008; Panagiotaki et al., 2012), which only chose parallel and perpendicular measurements to maximise sensitive to restricted diffusion. Our results confirm that these directions give the most information about the tissue, and one should focus on those directions when the fibre configuration is known *a-priori*.

We furthermore observe that our  $SF$  protocols contain slightly stronger diffusion weighting factors compared to the other protocols. We can attribute this to the custom gradient scheme, which translates to more measurements in the perpendicular direction and hence profits more from stronger diffusion attenuation than  $OL$ . The simulation results show the combination of stronger diffusion weighting and custom gradient scheme is superior in estimating the

cylinder radius, especially when  $R$  is very small.

Considering the few number of distinct gradient directions, it comes to no surprise that we found the optimised gradient schemes in  $\mathcal{SF}$  and  $\mathcal{SF}_{dirs}$  more prone to error when the true fibre orientation differs from the one assumed in the optimisation process. However, when the misalignment was less than  $15^\circ$  (as expected in coherent WM structures) the impact was negligible. We are confident that with careful positioning, the  $\mathcal{SF}$  gradient scheme can be aligned to the dominant fibre directions in CC and SC with little error without diminishing the performance of the  $\mathcal{SF}$  protocols.

Finally, the feasibility study on our post-mortem SC sample demonstrates that we can estimate a reasonable range of axon diameters and densities under realistic imaging conditions, while retaining a high image resolution. Furthermore we were able to distinguish different WM tracts of the SC by both axon diameter and axon density.

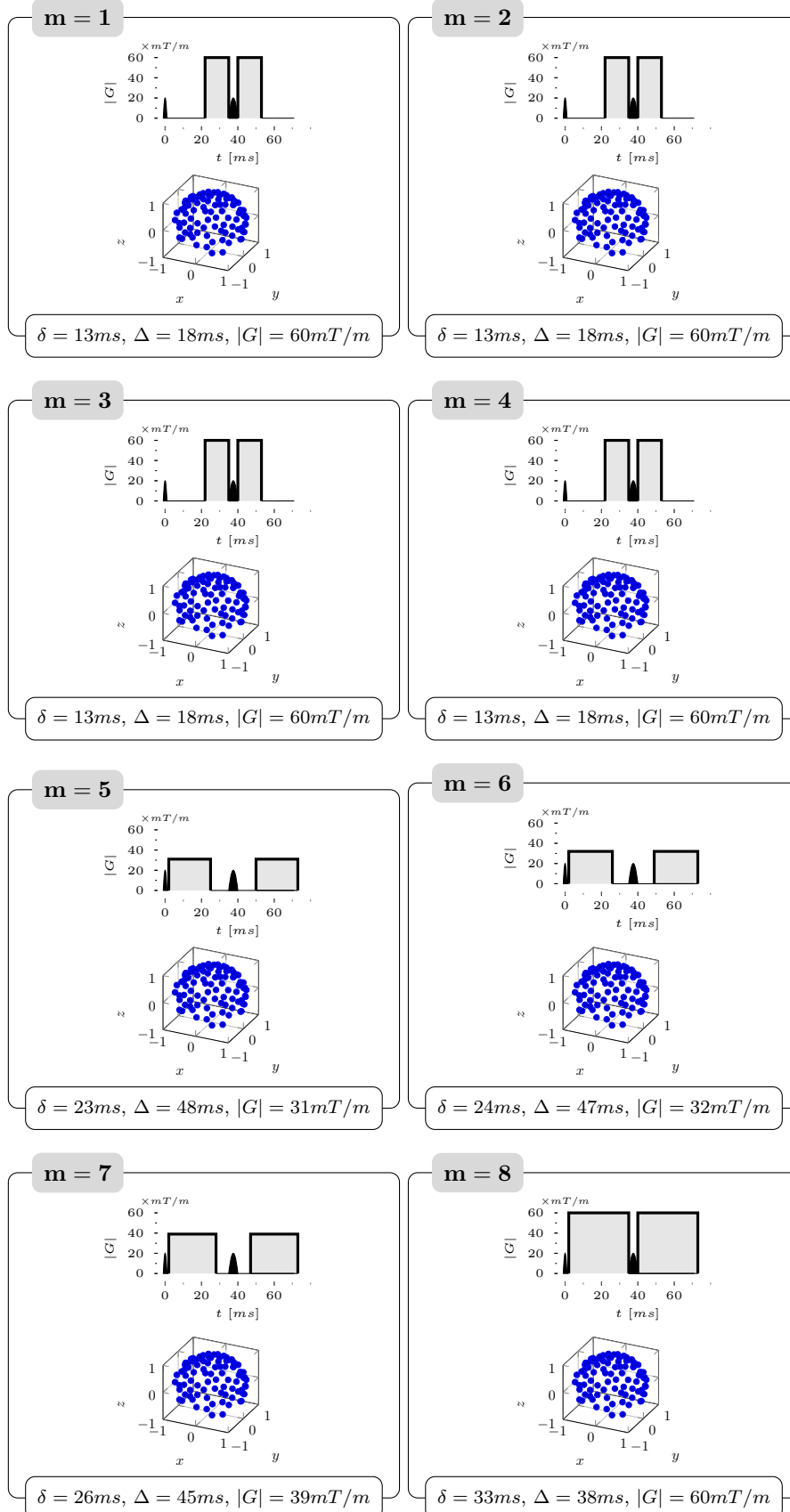
There are some limiting factors to our study. Firstly, we only optimise and fit a very simple tissue model, which only allows a crude approximation of the real tissue properties. Other, more complex, models might be a better representation of the real tissue microstructure, e.g. modelling explicitly a distribution of axon radii (Barazany et al., 2009) or including more extra-axonal tissue compartments (Stanisz et al., 1997; Wang et al., 2011; Panagiotaki et al., 2012). While these models might arguably be more accurate, they also require many more acquisitions and therefore do not agree with the aim of this study to reduce the scan time to less than 30 minutes. The choice of a simpler model offers a compromise of manageable data requirements and informative model parameters.

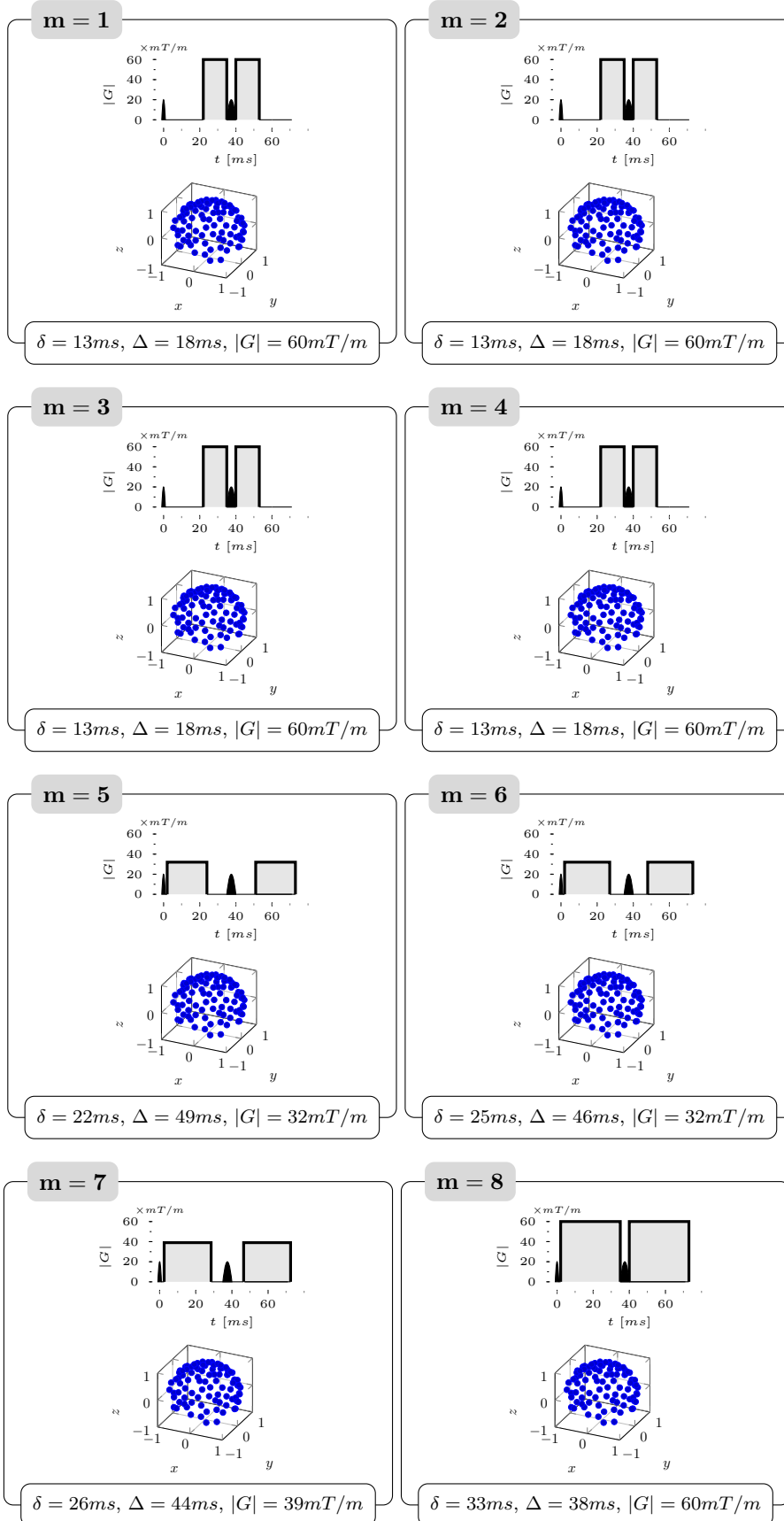
Secondly, the spinal cord sample we used in this study was not available for histological processing. Despite the lack of independent validation, the differences between WM tracts agree with previous results in (Golabchi et al., 2010). It should be noted that our results were obtained with a significantly smaller number of diffusion weighted directions and b-factors compared to other studies (Assaf et al., 2008; Barazany et al., 2009; Panagiotaki et al., 2012), making it more comparable to conditions found in in-vivo scanning. Nevertheless, in many this pre-clinical setup here has many advantages over the in-vivo situation, as it profits from long scan times, high SNR and an absence of motion artefacts. Although the findings in this experiment might therefore not be directly transferable to clinical practise, the results are encouraging enough to pursue the  $\mathcal{SF}$  approach in clinical practise. In the next two chapters we will therefore focus on moving the  $\mathcal{SF}$  approach to towards a feasible in-vivo implementation on standard clinical hardware.



## Appendix 1.A Protocols

### 1.A.1 Protocols optimised for $|G|_{max}=60mT/m$ , $N=90$ , $M=8$



Figure 1.11:  $\mathcal{SF}_{pulses}$  protocol optimised for clinical gradient strength

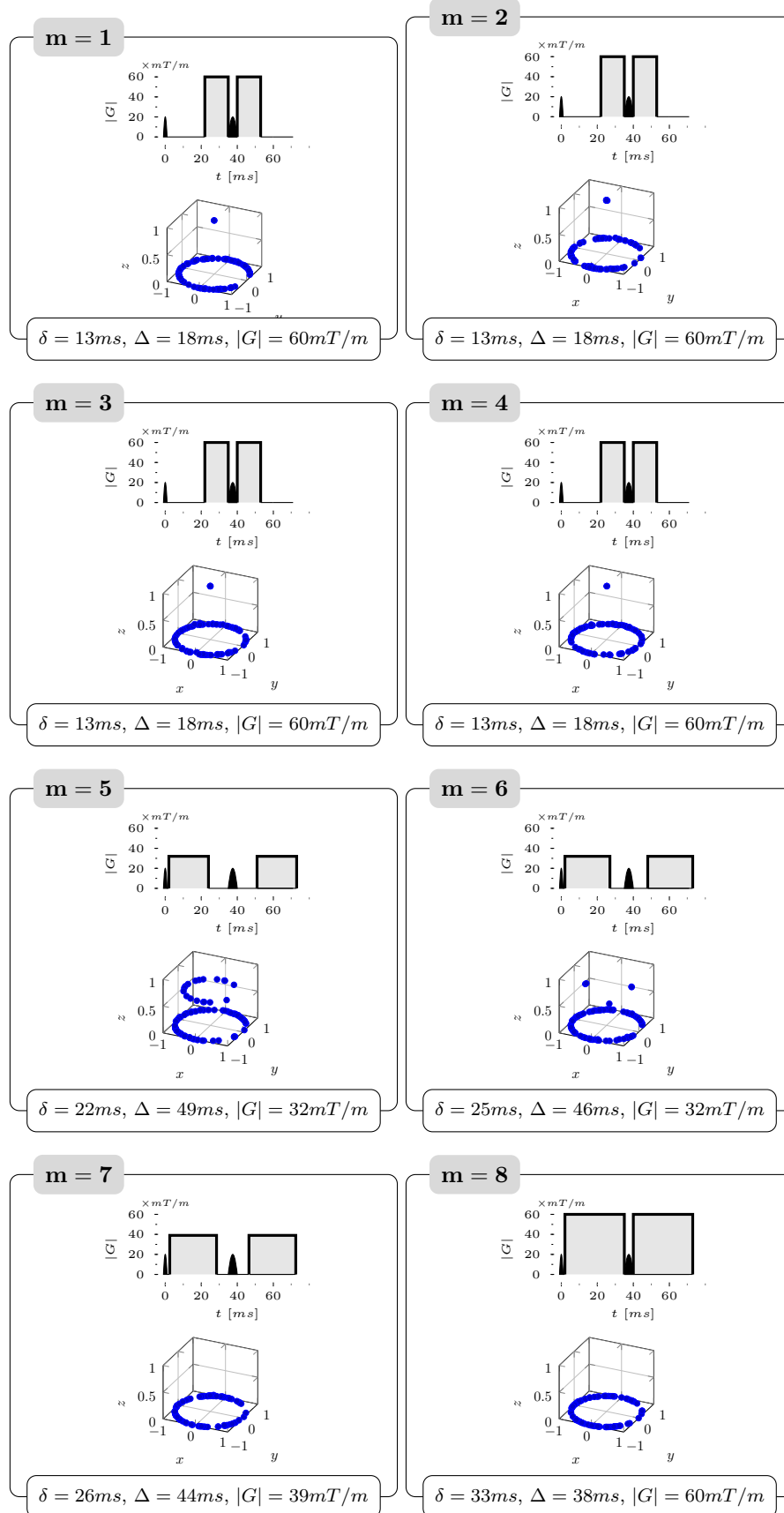
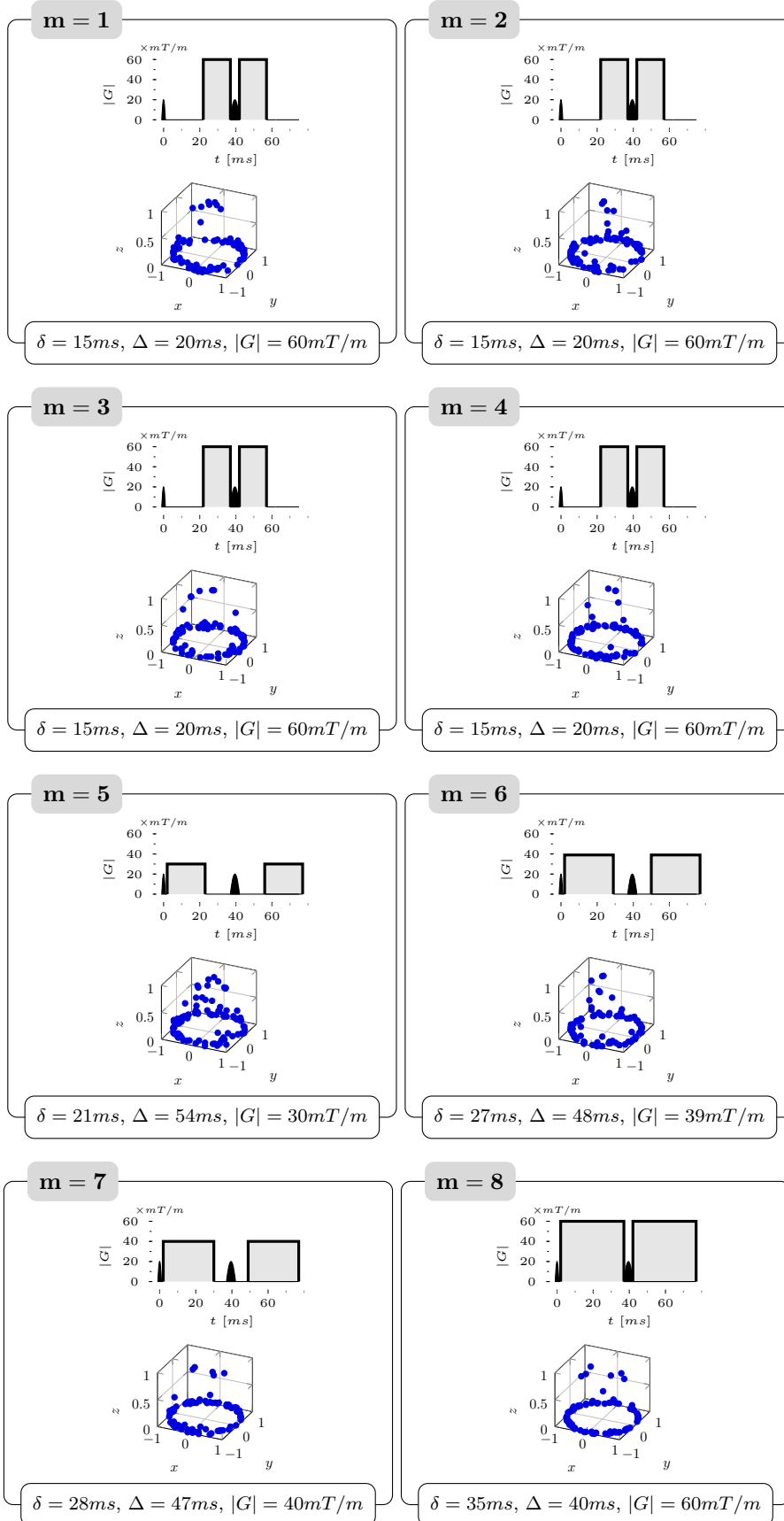
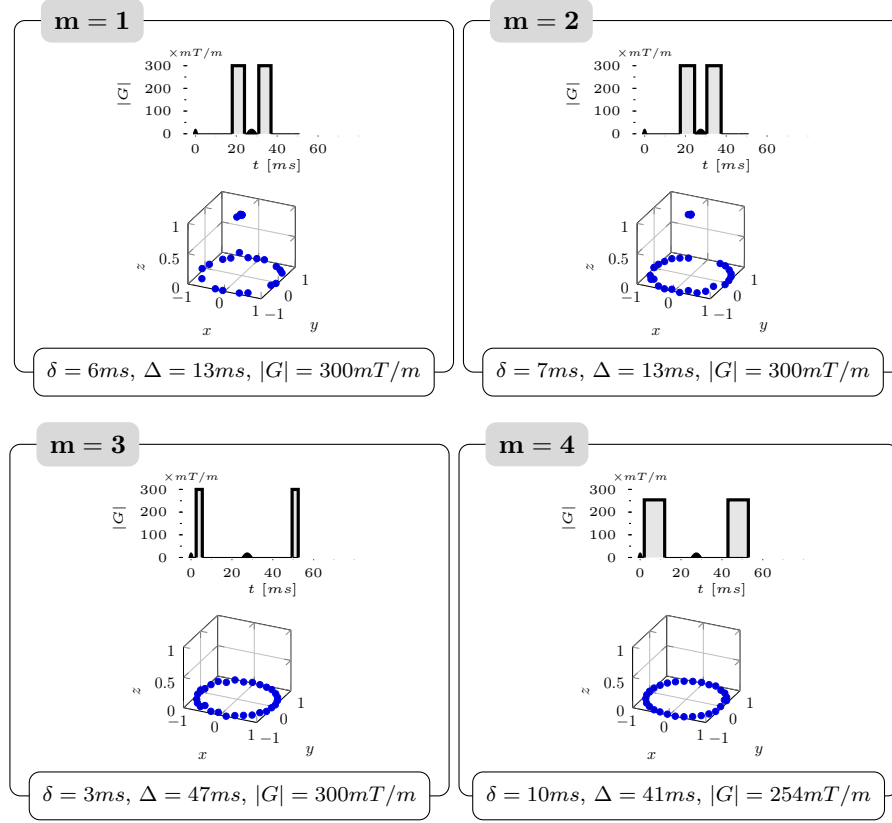


Figure 1.12:  $\mathcal{SF}_{dirs}$  protocol optimised for clinical gradient strength



Figure 1.13:  $\mathcal{SF}$  protocol optimised for clinical gradient strength

## 1.A.2 Pre-clinical scanner (300mT/m), N=30, M=4

Figure 1.14:  $\mathcal{SF}$  protocol optimised for pre-clinical scanner and fixed tissue.

# Bibliography

- Alexander, D. C. (2008). A general framework for experiment design in diffusion MRI and its application in measuring direct tissue-microstructure features. *Magnetic Resonance in Medicine*, 60(2), 439–448.
- Alexander, D. C., Hubbard, P. L., Hall, M. G., Moore, E. A., Ptito, M., Parker, G. J. M., & Dyrby, T. B. (2010). Orientationally invariant indices of axon diameter and density from diffusion MRI. *NeuroImage*.
- Assaf, Y., Blumenfeld-Katzir, T., Yovel, Y., & Basser, P. J. (2008). AxCaliber: a method for measuring axon diameter distribution from diffusion MRI. *Magnetic Resonance in Medicine*, 59(6), 1347–1354.
- Avram, L., Ā-zarslan, E., Assaf, Y., Bar-Shir, A., Cohen, Y., & Basser, P. J. (2008). Three-dimensional water diffusion in impermeable cylindrical tubes: theory versus experiments. *NMR Biomed.*, 21(8), 888–898.  
URL <http://dx.doi.org/10.1002/nbm.1277>
- Barazany, D., Basser, P. J., & Assaf, Y. (2009). In vivo measurement of axon diameter distribution in the corpus callosum of rat brain. *Brain*.
- Cook, P., Bai, Y., Nedjati-Gilani, S., Seunarine, K., Hall, M. G., Parker, G. J. M., & Alexander, D. C. (2006). Camino: open-source diffusion-MRI reconstruction and processing. In *Proceedings 14th Scientific Meeting, International Society for Magnetic Resonance in Medicine*, (p. 2759).
- Cook, P. A., Symms, M., Boulby, P. A., & Alexander, D. C. (2007). Optimal acquisition orders of diffusion-weighted MRI measurements. *Journal of Magnetic Resonance Imaging*, 25(5), 1051–1058.  
URL <http://dx.doi.org/10.1002/jmri.20905>
- Golabchi, F. N., Brooks, D. H., Hoge, W. S., Girolami, U. D., & Maier, S. E. (2010). Pixel-based comparison of spinal cord MR diffusion anisotropy with axon packing parameters. *Magnetic Resonance in Medicine*, 63(6), 1510–1519.
- Graf von Keyserlingk, D., & Schramm, U. (1984). Diameter of axons and thickness of myelin sheaths of the pyramidal tract fibres in the adult human medullary pyramid. *Anatomischer Anzeiger*, 157(2), 97–111.  
URL <http://ukpmc.ac.uk/abstract/MED/6507887>
- Panagiotaki, E., Schneider, T., Siow, B., Hall, M. G., Lythgoe, M. F., & Alexander, D. C. (2012). Compartment models of the diffusion MR signal in brain white matter: A taxonomy and comparison. *NeuroImage*, 59(3),

2241–2254.

URL <http://www.sciencedirect.com/science/article/pii/S1053811911011566>

Siow, B., Drobnjak, I., Chatterjee, A., Lythgoe, M. F., & Alexander, D. C. (2012). Estimation of pore size in a microstructure phantom using the optimised gradient waveform diffusion weighted NMR sequence. *Journal of Magnetic Resonance*, 214(0), 51–60.

URL <http://www.sciencedirect.com/science/article/pii/S1090780711003806>

Stanisz, G. J., Wright, G. A., Henkelman, R. M., & Szafer, A. (1997). An analytical model of restricted diffusion in bovine optic nerve. *Magnetic Resonance in Medicine*, 37(1), 103–111.

URL <http://onlinelibrary.wiley.com/doi/10.1002/mrm.1910370115/abstract>

Stejskal, E. O., & Tanner, J. E. (1965). Spin diffusion measurements: Spin echoes in the presence of a Time-Dependent field gradient. *Journal of Chemical Physics*, 42, 288.

Szafer, A., Zhong, J., Anderson, A. W., & Gore, J. C. (1995). Diffusion-weighted imaging in tissues: theoretical models. *NMR in Biomedicine*, 8(7-8), 289–296.

Wang, Y., Wang, Q., Halder, J. P., Yeh, F., Xie, M., Sun, P., Tu, T., Trinkaus, K., Klein, R. S., Cross, A. H., & Song, S. (2011). Quantification of increased cellularity during inflammatory demyelination. *Brain*, 134(12), 3590–3601.

URL <http://brain.oxfordjournals.org/content/134/12/3590>

Zhang, H., Hubbard, P. L., Parker, G. J., & Alexander, D. C. (2011). Axon diameter mapping in the presence of orientation dispersion with diffusion MRI. *NeuroImage*, 56(3), 1301–1315.

URL <http://www.sciencedirect.com/science/article/pii/S1053811911001376>